Computers and Structures 292 (2024) 107229

Contents lists available at ScienceDirect

Computers and Structures

journal homepage: www.elsevier.com/locate/compstruc

Data-driven characterization of viscoelastic materials using time-harmonic hydroacoustic measurements

Laura Río-Martín [b], A. Prieto [a,*]

[a] CITMAga, Departamento de Matemáticas, Universidade da Coruña, Spain
[b] Laboratory of Applied Mathematics, DICAM, University of Trento, Italy

ARTICLE INFO

Keywords:
Data-driven material characterization
Viscoelastic materials
Hydroacoustics
Young's modulus

ABSTRACT

Any numerical procedure in mechanics requires choosing an appropriate model for the constitutive law of the material under consideration. The most common assumptions regarding linear wave propagation in a viscoelastic material are the standard linear solid model, (generalized) Maxwell, Kelvin-Voigt models or the most recent fractional derivative models. Usually, once the frequency-dependent constitutive law is fixed, the intrinsic parameters of the mathematical model are estimated to fit the available experimental data with the mechanical response of that model. This modelling methodology potentially suffers from the epistemic uncertainty of an inadequate a priori model selection. However, in this work, the mathematical modelling of linear viscoelastic materials and the choice of their frequency-dependent constitutive laws is performed based only on the available experimental measurements without imposing any functional frequency dependence. This data-driven approach requires the numerical solution of an inverse problem for each frequency. The acoustic response of a viscoelastic material due to the time-harmonic excitations has been calculated numerically. In these numerical simulations, the non-planar directivity pattern of the transducer has been taken into account. Experimental measurements of insertion loss and fractional power dissipation in underwater acoustics have been used to illustrate the data-driven methodology that avoids selecting a parametric viscoelastic model.

1. Introduction

Elastomeric materials appear in many automotive, aerospace, or naval applications because they can be used in passive structural vibration control or noise radiation techniques [31,37,39,40]. These materials are polymers with a viscoelastic mechanical behaviour at ultrasound frequencies [17,25]. In fact, the continuous arising of new materials in biomedical applications or agri-food industries [32], many of them with unknown properties, or the characterization of biological tissues, such as human aortas [3,19,20], makes a complete description of their mechanical behaviour necessary. In the present work, a polymeric material with a planar surface has been numerically characterized by using the frequency response of the insertion loss and the fractional power dissipation at ultrasonic frequencies.

A suitable choice of the viscoelastic model is fundamental to performing the material characterization: the more appropriate the model is, the more accurate its mechanical response will be, compared with the experimental data. Well-known viscoelastic material models such as the standard linear solid model or the (generalized) Maxwell, Zener, and Kelvin-Voigt models [10,18,33], or the more recent fractional derivative viscoelasticity models [4,27] are common choices for modelling linear wave propagation in viscoelastic materials. Usually, to estimate the unknown parameters, the constitutive laws are first fixed, and then the available experimental data are fitted with the response of the mathematical model. However, in the present work, a data-driven approach is considered [14,21,28]. This methodology avoids the need to choose a parametric constitutive law for fitting. Instead, an inverse problem consists of minimizing the distance between a set of experimental data and the computed values is solved numerically. Therefore, the choice of the viscoelastic model is based only on the experimental ultrasound measurements and not on imposing any functional dependence on the parameters in terms of frequency.

In this work, a viscoelastic material has been characterized using a data-driven approach instead of a classical parametric model. This material is part of a coupled problem formed by the material surrounded by water. In Section 2, an analysis of the mathematical modelling of the

* Corresponding author.
E-mail addresses: laura.delrio@unitn.it (L. Río-Martín), andres.prieto@udc.es (A. Prieto).

https://doi.org/10.1016/j.compstruc.2023.107229
Received 21 December 2022; Accepted 9 November 2023
Available online 22 November 2023

problem has been performed. First, Section 2.1 describes the mathematical models of the problem under consideration, including the classical parametric models, emphasizing the differences between the parametric and the non-parametric approaches. Then, the coupled problem under consideration is described, and the acoustic quantities of interest, such as the reflection and the transmission coefficients, the insertion loss, and the fractional power dissipation, are defined. The direct problem of wave propagation in the multilayer medium is described in Section 3. A complete description of the pressure fields (incident, reflected, and transmitted) by using an integral representation is given in Section 3.1. Then, Section 3.2 is devoted to the computation of the reflection and the transmission coefficients in a plane wave framework. In Section 4, the inverse problems for parametric and non-parametric approaches are described, taking into account different constitutive laws for the primal unknowns of the fitting problem, and emphasizing the advantages and disadvantages of each methodology. When the real and imaginary parts of the Young's modulus are used as unknowns, the frequency response of the levels under consideration presents spurious oscillations. Therefore, a change in the primal unknowns is necessary, and the fitting problem writing with these new unknowns is described. Since a trust-region reflective algorithm is used to solve the inverse fitting problems, and this optimization algorithm needs the evaluation of the first-order derivatives of the cost function. Section 5 is devoted to presenting some numerical results. More precisely, numerical simulations with manufactured data are shown in Section 5.1 to validate the code implementation of this data-driven approach. Then, a real-world viscoelastic material is characterized by using the proposed methodology. In Section 5.2, the available experimental data are presented. Sections 5.3 and 5.4 show the numerical results obtained using parametric and non-parametric approaches, respectively which enables the analysis of the robustness and efficiency of the data-driven approach. Section 6 summarizes the conclusions about this proposed methodology.

Remark 1.1. *Throughout the present work, the time-harmonic dependence for the pressure field (and for the displacement field) has been settled as* $p(\boldsymbol{x},t)=\mathrm{Re}(P(\boldsymbol{x})e^{-i\omega t})$*, being* p *the time-dependent acoustic pressure field,* P *the complex-valued time-harmonic acoustic pressure field,* ω *the angular frequency,* t *the time variable,* $\boldsymbol{x}$ *the Cartesian coordinates of the spatial position,* $\mathrm{Re}(\cdot)$ *the real part function of a complex number, and* i *the imaginary unit.*

2. Mathematical modelling

A coupled fluid-structure problem has been considered to characterize the viscoelastic material. Then, in this section, the mathematical models of the layers involved in the coupled problem are described in detail, and finally, the acoustic quantities of interest in this material characterization approach are defined.

2.1. Mathematical models

The coupled problem under study involves the vibroacoustic interaction between a viscoelastic solid with finite thickness and a compressible dissipative fluid surrounding it. In what follows, the mechanical models governing both media are described in detail.

2.1.1. Compressible dissipative fluid

Taking into account the fluid dissipation (see [36] for further details) and considering the acoustic pressure field p as the primal unknown, the time-dependent equation of motion of a compressible dissipative fluid (which is assumed isentropic) is given by

$$\frac{1}{\rho_{\mathrm{F}}c_{\mathrm{F}}^2}\frac{\partial^2 p}{\partial t^2}+\frac{\alpha^2}{\rho_{\mathrm{F}}}\frac{\partial^4 p}{\partial t^4}+\frac{2\alpha}{\rho_{\mathrm{F}}c_{\mathrm{F}}}\frac{\partial^3 p}{\partial t^3}-\mathrm{div}\left(\frac{1}{\rho_{\mathrm{F}}}\nabla p\right)=0,$$

where α is the attenuation coefficient, and ρ_{F} and c_{F} are the mass density and the sound speed of the fluid, respectively. Assuming harmonic solutions, $p(\boldsymbol{x},t)=\mathrm{Re}(e^{-i\omega t}P(\boldsymbol{x}))$, the motion equation is given by

$$-\frac{\omega^2}{\rho_{\mathrm{F}}c_{\mathrm{F}}^2}P+\frac{\alpha^2\omega^4}{\rho_{\mathrm{F}}}P+\frac{2i\alpha\omega^3}{\rho_{\mathrm{F}}c_{\mathrm{F}}}P-\mathrm{div}\left(\frac{1}{\rho_{\mathrm{F}}}\nabla P\right)=0.$$

If it is assumed that the fluid is homogeneous, this is, ρ_{F} is constant, and taking into account $\mathrm{div}\,\nabla P=\Delta P$, it holds

$$\left[-\frac{\omega^2}{c_{\mathrm{F}}^2}+\alpha^2\omega^4+\frac{2i\alpha\omega^3}{c_{\mathrm{F}}}\right]P-\Delta P=-\left[\frac{\omega}{c_{\mathrm{F}}}-i\alpha\omega^2\right]^2P-\Delta P=0. \tag{1}$$

Hence, the dissipative time-harmonic model (1) can be written as

$$-k_{\mathrm{F}}^2(\omega)P-\Delta P=0, \tag{2}$$

which is the so-called Helmholtz equation with a complex-valued wavenumber given by $k_{\mathrm{F}}(\omega)=\omega/c_{\mathrm{F}}-i\alpha\omega^2$.

2.1.2. Viscoelastic solid

Under the small deformations hypothesis (see [30]), the time-dependent linear equation of motion for a viscoelastic solid (which is assumed homogeneous and isotropic), written in terms of the displacement, is given by

$$\rho_{\mathrm{V}}\frac{\partial^2\boldsymbol{u}_{\mathrm{V}}}{\partial t^2}-\mathrm{div}(\boldsymbol{\sigma})=\boldsymbol{0},$$

where ρ_{V} is the mass density at the equilibrium state of reference, $\boldsymbol{u}_{\mathrm{V}}$ is the displacement field, and $\boldsymbol{\sigma}$ is the stress tensor. Moreover, if the strain is sufficiently small, the mechanical behaviour of the viscoelastic solid can be described accurately using a linear dependency between strains and stresses in the material. From a general point of view, the linear constitutive relation between the stress and the strain tensor in the viscoelastic solid (see [22]) can be written as the time convolution product

$$\sigma_{ij}(\boldsymbol{x},t)=\int_{-\infty}^{t}\mathsf{c}_{ijkl}(t-\tau)\frac{\partial\varepsilon_{kl}}{\partial t}(\boldsymbol{x},\tau)\mathrm{d}\tau, \tag{3}$$

where $\varepsilon=(\nabla\boldsymbol{u}_{\mathrm{V}}+\nabla\boldsymbol{u}_{\mathrm{V}}^t)/2$ is the strain tensor, and c is the viscoelasticity tensor. If a time-harmonic dependency is prescribed formally on the viscoelastic model, this is, $\mathsf{c}(t)=\mathrm{Re}(e^{-i\omega t}\mathsf{C}(\omega))$, $\boldsymbol{u}_{\mathrm{V}}(\boldsymbol{x},t)=\mathrm{Re}(e^{-i\omega t}\boldsymbol{U}_{\mathrm{V}}(\boldsymbol{x}))$, and $\varepsilon(\boldsymbol{x},t)=\mathrm{Re}(e^{-i\omega t}\Sigma(\boldsymbol{U}_{\mathrm{V}}))$ with $\Sigma(\boldsymbol{U}_{\mathrm{V}})=(\nabla\boldsymbol{U}_{\mathrm{V}}+\nabla\boldsymbol{U}_{\mathrm{V}}^t)/2$, then it can be deduced from (3) that

$$\sigma(\boldsymbol{x},t)=\mathrm{Re}(e^{-i\omega t}\mathsf{C}(\omega)\Sigma(\boldsymbol{U}_{\mathrm{V}}(\boldsymbol{x}))).$$

Hence, the time-harmonic displacement field satisfies the following motion equation:

$$-\omega^2\rho_{\mathrm{V}}\boldsymbol{U}_{\mathrm{V}}-\mathrm{div}(\mathsf{C}(\omega)\Sigma(\boldsymbol{U}_{\mathrm{V}}))=\boldsymbol{0}.$$

If the viscoelastic material is assumed isotropic, it is straightforward to show using the principle of indifference material (see Gurtin [22]) that the coefficients of the viscoelasticity tensor are given by

$$\mathsf{C}_{ijkl}(\omega)=\lambda(\omega)\delta_{ij}\delta_{kl}+\mu(\omega)(\delta_{ik}\delta_{jl}+\delta_{il}\delta_{jk}), \tag{4}$$

where $\lambda(\omega)$ and $\mu(\omega)$ are the Lame's coefficients and δ_{ij} denotes the Kronecker's delta. For simplicity but without losing generality on the proposed approach, the Poisson's ratio ν is considered a real-valued constant and the Young's modulus $E(\omega)$ is an arbitrary complex-valued frequency-dependent function in such a manner that the Lame's coefficients are written as follows:

$$\lambda(\omega)=\frac{\nu E(\omega)}{(1-2\nu)(1+\nu)},\qquad \mu(\omega)=\frac{E(\omega)}{(1+\nu)}. \tag{5}$$

Two different approaches can be followed to choose the constitutive law for the viscoelasticity tensor attending to the definition of $E(\omega)$: a

parametric approach using well-known models, such as the Maxwell or the Kelvin-Voigt model, or a non-parametric methodology where it is not required an *a priori* knowledge of the frequency-dependent constitutive relations between strains and stresses in the material. Following [9], a formal definition of these two methodologies in the framework of the mathematical modelling of viscoelastic materials is given in what follows.

Definition 2.1. *The frequency-dependent values of the real and the imaginary part of the Young's modulus, respectively $E'(\omega)$ and $E''(\omega)$, involved in a viscoelastic model follows:*

i) *A parametric approach if there exist two response functions $\hat{E}'$ and $\hat{E}''$ (known in closed-form) and a finite number of constant parameters $a_1,\dots,a_m$ such that $\hat{E}' : (a_1,\dots,a_m) \mapsto \hat{E}'(a_1,\dots,a_m) \in C(0,\infty)$ and $\hat{E}'' : (a_1,\dots,a_m) \mapsto \hat{E}''(a_1,\dots,a_m) \in C(0,\infty)$, and it holds*

$$E'(\omega) = [\hat{E}'(a_1,\dots,a_m)](\omega), \qquad E''(\omega) = [\hat{E}''(a_1,\dots,a_m)](\omega).$$

ii) *A non-parametric approach if both values $E'(\omega)$ and $E''(\omega)$ are only assumed given by arbitrary real-valued continuous functions, this is, $E', E'' \in C(0,\infty)$.*

Among the classical parametric viscoelastic models, the Kelvin-Voigt model will be used throughout this manuscript for comparison purposes with respect the proposed non-parametric approach. In this particular case, (3) can be rewritten (see [34]) into a simpler differential constitutive equation for the stress tensor given by

$$\sigma_{ij} = \mathrm{c}^{\mathrm{E}}_{ijkl}\left(\varepsilon_{kl} + \eta\dot{\varepsilon}_{kl}\right),$$

where $\mathrm{c}^{\mathrm{E}}_{ijkl}$ is the classical elasticity tensor (with constant real-valued Young's modulus E and Poisson's ratio ν) and η is the so-called loss factor. Consequently, in the time-harmonic regime, σ can be rewritten in terms of C (defined in (4)) with $E(\omega) = E(1-i\omega\eta)$. Hence, the Kelvin-Voigt model follows Definition 2.1 with two constant parameters $a_1 = E$ and $a_2 = \eta$ such that $\hat{E}'(E,\eta) = E$ and $\hat{E}''(E,\eta) = \omega\eta E$.

2.2. Viscoelastic-fluid coupled problem

Once the mathematical models of the media involved in the problem under study have been introduced, a multilayer planar configuration formed by a viscoelastic solid surrounded by a compressible dissipative fluid (water in the case under study) is considered. Let Ω_{F} and Ω_{B} be the domains occupied by the fluid in the front and back of the viscoelastic layer, which is located in Ω_{V}. Both fluid media are placed on unbounded domains (half-spaces), and the thickness of the viscoelastic layer is finite (denoted by l) but unbounded in the other two Cartesian coordinates. The coupled interfaces Γ_{F} and Γ_{B} denotes the front and back planar surfaces of the viscoelastic layer located on the planes $x_3 = -l/2$ and $x_3 = l/2$. Both interfaces are perpendicular to the Cartesian x_3-axis, so the unit normal vector on Γ_{F} and Γ_{B} is $\boldsymbol{n} = \boldsymbol{e}_1$. On both interfaces, kinetic and kinematic coupled conditions are considered to preserve the continuity of normal displacements and normal tensions. To write the formulation of the coupled problem, the equation of motion of the compressible fluid has been expressed in terms of the pressure field and the equation of motion of the viscoelastic model in terms of the displacement field. This coupled problem is given by: for a fixed angular frequency $\omega > 0$, find the acoustic pressure fields in the first and last fluid P_{F} and P_{B}, and the displacement field $\boldsymbol{U}_{\mathrm{V}}$ in the viscoelastic medium such that

$$\begin{cases} -k_{\mathrm{F}}^2(\omega)P_{\mathrm{F}} - \Delta P_{\mathrm{F}} = 0 & \text{in } \Omega_{\mathrm{F}}, \\ -\omega^2\rho_{\mathrm{V}}\boldsymbol{U}_{\mathrm{V}} - \mathrm{div}(\mathsf{C}(\omega)\Sigma(\boldsymbol{U}_{\mathrm{V}})) = \boldsymbol{0} & \text{in } \Omega_{\mathrm{V}}, \\ -k_{\mathrm{F}}^2(\omega)P_{\mathrm{B}} - \Delta P_{\mathrm{B}} = 0 & \text{in } \Omega_{\mathrm{B}}, \\ \boldsymbol{U}_{\mathrm{F}}\cdot\boldsymbol{n} = \boldsymbol{U}_{\mathrm{V}}\cdot\boldsymbol{n} & \text{on } \Gamma_{\mathrm{F}}, \\ -P_{\mathrm{F}} = (\mathsf{C}(\omega)\Sigma(\boldsymbol{U}_{\mathrm{V}}))\boldsymbol{n}\cdot\boldsymbol{n} & \text{on } \Gamma_{\mathrm{F}}, \\ \boldsymbol{U}_{\mathrm{V}}\cdot\boldsymbol{n} = \boldsymbol{U}_{\mathrm{B}}\cdot\boldsymbol{n} & \text{on } \Gamma_{\mathrm{B}}, \\ (\mathsf{C}(\omega)\Sigma(\boldsymbol{U}_{\mathrm{V}}))\boldsymbol{n}\cdot\boldsymbol{n} = -P_{\mathrm{B}} & \text{on } \Gamma_{\mathrm{B}}, \end{cases} \tag{6}$$

where $\boldsymbol{U}_j = -\omega\rho_{\mathrm{F}}/k_{\mathrm{F}}(\omega)\nabla P_j$ is the displacement field in the fluid domain Ω_j with $j = \mathrm{F},\mathrm{B}$, and $\Sigma(\boldsymbol{U}_{\mathrm{V}})$ is the strain tensor of the viscoelastic medium. Additionally, to guarantee no scattering waves are coming from the second fluid towards the viscoelastic solid, convenient radiation conditions involving an incident pressure field should be additionally imposed on the pressure fields P_{F} and P_{B} at infinity.

2.3. Acoustic quantities of interest

In this section, some coefficients and levels of interest for the problem under study are defined. Since an underwater environment is considered, the acoustic pressure field is measured using hydrophones located at a spatial point $\boldsymbol{x}$. The total pressure fields P_{F} and P_{B} are decomposed taking into account the incident pressure field impinging the viscoelastic layer from the fluid domain Ω_{F}. In this manner, $P_{\mathrm{F}} = P_{\mathrm{rf}} + P_{\mathrm{in}}$, where P_{in} is the incident pressure and P_{rf} is the reflected pressure field, and $P_{\mathrm{B}} = P_{\mathrm{tr}}$ is the transmitted pressure field to the fluid domain Ω_{B}. The magnitude of the incident pressure field evaluated at a fixed point $\boldsymbol{x}_{\mathrm{F}} \in \Omega_{\mathrm{F}}$ will be used to obtain a normalized quantification of the reflected and transmitted pressure fields.

Definition 2.2 *(Reflection coefficient). The reflection coefficient is the ratio of the reflected pressure to the incident pressure, that is,*

$$\mathcal{R}(\boldsymbol{x}) = \frac{P_{\mathrm{rf}}(\boldsymbol{x})}{P_{\mathrm{in}}(\boldsymbol{x}_{\mathrm{F}})}, \qquad \boldsymbol{x} \in \Omega_{\mathrm{F}}, \tag{7}$$

where recall P_{rf} and P_{in} are the acoustic pressure reflected from the viscoelastic layer and the incident acoustic pressure field, respectively, measured at a point located in the front fluid domain.

Definition 2.3 *(Transmission coefficient). The transmission coefficient is defined as the ratio of the transmitted pressure to the incident pressure,*

$$\mathcal{T}(\boldsymbol{x}) = \frac{P_{\mathrm{tr}}(\boldsymbol{x})}{P_{\mathrm{in}}(\boldsymbol{x}_{\mathrm{F}})}, \qquad \boldsymbol{x} \in \Omega_{\mathrm{B}}, \tag{8}$$

where P_{tr} is the acoustic pressure transmitted through the viscoelastic layer and P_{in} is the acoustic incident pressure impinging it from the front fluid

If the acoustic transducer used to generate the incident wave and the hydrophones are aligned (on the x_3-axis), the incident field is axisymmetric with respect to the x_3-axis, and taking into account that the viscoelastic layer is placed between the planes $x_3 = -l/2$ and $x_3 = l/2$ then the definition of the levels can be written in terms of x_3 and evaluated on the coupling interfaces Γ_{F} and Γ_{B} as follows.

Definition 2.4 *(Insertion Loss). The Insertion Loss (IL) associated with the viscoelastic layer is defined by*

$$\mathrm{IL} = -20\log_{10}|\mathcal{T}(0,0,l/2)|, \tag{9}$$

where $\mathcal{T}$ is the transmission coefficient defined in (8).

Definition 2.5 *(Fractional Power Dissipation). The Fractional Power Dissipation (FPD) is given by*

$$\mathrm{FPD} = 1 - |\mathcal{R}(0,0,-l/2)|^2 - |\mathcal{T}(0,0,l/2)|^2, \tag{10}$$

where $\mathcal{R}$ and $\mathcal{T}$ are the reflection and the transmission coefficients, respectively. (See Fig. 1.)

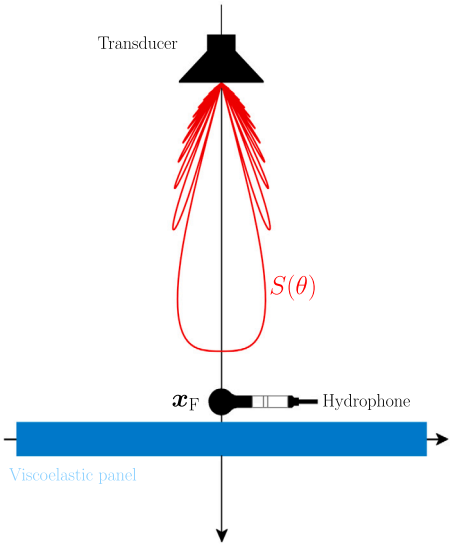

Fig. 1. Experimental setup used to measure the incident, reflected, and transmitted pressure fields. The viscoelastic material is highlighted in blue. $x_{3\mathrm{m}}$ is the hydrophone position in the x_3-axis. Depending on the measured coefficient, the hydrophone may be located in front or back of the viscoelastic layer. The directivity pattern $S(\theta)$ is highlighted in red.

Remark 2.6. *All the physical quantities of interest (i.e.,* ER*,* IL*, and* FPD*) introduced in this work are obtained under the small perturbations assumption, where the vibroacoustic behaviour of the viscoelastic material is linear. Otherwise, in the case of large mechanical perturbations of the material, where its mechanical response is non-linear, the hysteresis loop could be used to quantify the storage modulus and the loss factor of the viscoelastic model (see [19]).*

3. Statement of the direct problem

The frequency response data of the insertion loss and the fractional power dissipation have been considered to obtain a complete characterization of the constitutive law associated with the viscoelastic material. These available experimental data have been measured in an NPL Acoustic Pressure Vessel using a parametric array as the acoustic source [5]. Hence, the acoustic pressure field must be represented, taking into account the directivity pattern of this acoustic source. This section describes an integral representation of the incident, reflected, and transmitted pressure fields. For completeness, the computation of the reflection and the transmission coefficients involved in that integral representation is described in detail in a plane wave framework.

3.1. Integral representation of pressure fields

The incident, reflected, and transmitted pressure fields are represented utilizing a complex-path integral over the plane wave spectrum. When an arbitrary incident wave (different from plane waves) impinges into a planar interface between two media, the numerical computation of the reflected and transmitted waves is challenging due to the application of the coupling conditions among media and the lack of symmetry between the incident wave and the geometry of the coupling boundaries. However, any arbitrary impinging wave can be expanded into plane waves using an integral representation [8] to overcome these numerical difficulties. In what follows, the media are assumed dissipative compressible fluids to ensure that the wavenumber k is complex-valued. Such a feature implies that the fundamental solutions (spherical waves) in (2) associated with those fluid media are spatially damped and belong to $\mathrm{L}^2(\mathbb{R}^3)$. Consequently, a Fourier analysis approach can be applied in this context rigorously. Hence, following [8] if θ and ϕ denote the angles in spherical coordinates, any arbitrary incident pressure field with a given plane wave spectrum $S(\theta,\phi)$ can be represented by

$$P_{\mathrm{in}}(\boldsymbol{x}) = \frac{ik_{\mathrm{F}}}{2p}\int_0^{\frac{\pi}{2}-i\infty}\int_0^{2\pi} S(\theta,\phi)e^{i\boldsymbol{k}\cdot\boldsymbol{x}}\sin\theta\,\mathrm{d}\phi\,\mathrm{d}\theta, \tag{11}$$

where $\boldsymbol{k} = k_{\mathrm{F}}(\cos\phi\sin\theta, \sin\phi\sin\theta, \cos\theta)^t$. In the case of a parametric array of length h and the plane wave spectrum $S(\theta,\phi)$ is given by

$$S(\theta,\phi) = Q_0\frac{e^{ik_{\mathrm{F}}h(1-\cos\theta)}-1}{ik_{\mathrm{F}}(1-\cos\theta)}, \tag{12}$$

that is, the plane wave spectrum is a function of θ only. Then, the spatial point on the x_3-axis in front of the viscoelastic layer and the axis-symmetry of the incident acoustic field about the x_3-axis, the incident pressure field, given by (11), can be written as

$$P_{\mathrm{in}}(\boldsymbol{x}) = ik_{\mathrm{F}}\int_0^{\frac{\pi}{2}-i\infty} S(\theta)e^{ik_{\mathrm{F}}x_3\cos\theta}\sin\theta\,\mathrm{d}\theta. \tag{13}$$

Following a similar argument, the transmitted acoustic pressure field, P_{tr}, at a spatial point $\boldsymbol{x}$ placed on the back of the viscoelastic layer, can be calculated by integrating over the transmitted field components (see [23]), that is,

$$P_{\mathrm{tr}}(\boldsymbol{x}) = ik_{\mathrm{F}}\int_0^{\frac{\pi}{2}-i\infty} S(\theta)\mathcal{T}(\boldsymbol{x})e^{ik_{\mathrm{F}}x_3\cos\theta}\sin\theta\,\mathrm{d}\theta, \tag{14}$$

where $S(\theta)$ is the plane wave spectrum given by (12). Analogously, the reflected pressure field P_{rf} at a spatial point $\boldsymbol{x}$ in front of the sample can be calculated by integrating over the reflected field components and so it holds

$$P_{\mathrm{rf}}(\boldsymbol{x}) = ik_{\mathrm{F}}\int_0^{\frac{\pi}{2}-i\infty} S(\theta)\mathcal{R}(\boldsymbol{x})e^{ik_{\mathrm{F}}x_3\cos\theta}\sin\theta\,\mathrm{d}\theta, \tag{15}$$

where the plane wave spectrum $S(\theta)$ is given by (12).

3.2. Computation of reflection and transmission coefficients by using a plane wave framework

Integral expressions used to compute reflected and transmitted pressure fields described in the section above involve the reflection and transmission coefficients for an oblique incident wave. For a given fixed angle of incidence θ, these coefficients can be computed in closed form using a plane wave analysis of a multilayer structure formed by the front and back fluid surrounding the viscoelastic layer. Suppose an incident plane wave is impinging on the viscoelastic layer with an incidence angle θ_{F}. In this case, the complex-valued displacement in each medium is given by a linear combination of transmitted and reflected plane waves. More precisely, the displacement fields in both fluids are given only by a linear combination of longitudinal waves. However, straightforward computations show that the displacement field in the viscoelastic solid is given not only by longitudinal waves but also by transversal waves.

In the frequency domain, the displacement field in both fluids (front and back media labelled with the subscripts F and B, respectively) at oblique incidence can be written as

$$\boldsymbol{U}_j(\boldsymbol{x}) = A_j e^{ik_{\mathrm{F}}\boldsymbol{d}_j^-\cdot\boldsymbol{x}}\boldsymbol{d}_j^- + B_j e^{ik_{\mathrm{F}}\boldsymbol{d}_j^+\cdot\boldsymbol{x}}\boldsymbol{d}_j^+, \quad j=\mathrm{F},\mathrm{B},$$

where A_j and B_j with $j=\mathrm{F},\mathrm{B}$, are frequency-dependent complex constants which can be viewed as the reflection and transmission coefficients between each medium, θ_{F} and θ_{B} are the incident angles in the first and the last fluid, respectively, k_{F} is the wavenumber of the fluid, given by $k_{\mathrm{F}} = \omega/c_{\mathrm{F}}$, being c_{F} the sound velocity in the fluid,

$$\boldsymbol{d}_j^- = \begin{pmatrix} -\cos\theta_j \\ \sin\theta_j \end{pmatrix} \quad \text{and} \quad \boldsymbol{d}_j^+ = \begin{pmatrix} \cos\theta_j \\ \sin\theta_j \end{pmatrix}, \qquad j = \mathrm{F}, \mathrm{B}.$$

Since the pressure field is defined as $P_j = -\rho_{\mathrm{F}} c_{\mathrm{F}}^2 \operatorname{div} \boldsymbol{U}_j, \quad j = \mathrm{F}, \mathrm{B}$, the pressure field of both fluids P_j with $j = \mathrm{F}, \mathrm{B}$, at oblique incidence can be written as

$$P_j(\boldsymbol{x}) = -i\omega Z_{\mathrm{F}} \left(A_j e^{ik_{\mathrm{F}} \boldsymbol{d}_j^- \cdot \boldsymbol{x}} + B_j e^{ik_{\mathrm{F}} \boldsymbol{d}_j^+ \cdot \boldsymbol{x}} \right),$$

being Z_{F} the characteristic impedance of the medium, given by $Z_{\mathrm{F}} = \rho_{\mathrm{F}} c_{\mathrm{F}}$.

The displacement field of a viscoelastic solid $\boldsymbol{U}_{\mathrm{V}}$ is given by a linear combination of longitudinal waves, where the oscillations occur in the direction of wave propagation, and transverse waves, where the particle displacement due to the plane wave is perpendicular to the direction of propagation. Then the displacement field at oblique incidence can be written as

$$\begin{aligned} \boldsymbol{U}_{\mathrm{V}}(\boldsymbol{x}) &= \boldsymbol{U}_{\mathrm{V_l}}(\boldsymbol{x}) + \boldsymbol{U}_{\mathrm{V_t}}(\boldsymbol{x}) \\ &= A_{\mathrm{V_l}} e^{ik_{\mathrm{V_l}} \boldsymbol{d}_{\mathrm{l}}^- \cdot \boldsymbol{x}} \boldsymbol{d}_{\mathrm{l}}^- + B_{\mathrm{V_l}} e^{ik_{\mathrm{V_l}} \boldsymbol{d}_{\mathrm{l}}^+ \cdot \boldsymbol{x}} \boldsymbol{d}_{\mathrm{l}}^+ + A_{\mathrm{V_t}} e^{ik_{\mathrm{V_t}} \boldsymbol{d}_{\mathrm{t}}^- \cdot \boldsymbol{x}} \left(\boldsymbol{d}_{\mathrm{t}}^-\right)^{\perp} \\ &\quad + B_{\mathrm{V_t}} e^{ik_{\mathrm{V_t}} \boldsymbol{d}_{\mathrm{t}}^+ \cdot \boldsymbol{x}} \left(\boldsymbol{d}_{\mathrm{t}}^+\right)^{\perp}, \end{aligned}$$

where $A_{\mathrm{V_l}}$, $B_{\mathrm{V_l}}$, $A_{\mathrm{V_t}}$, and $B_{\mathrm{V_t}}$, are frequency-dependent complex constants that can be viewed as the reflection and transmission coefficients inside the viscoelastic layer, $\theta_{\mathrm{V_l}}$ and $\theta_{\mathrm{V_t}}$ are the incident angles of the longitudinal and transverse waves in the viscoelastic solid, $k_{\mathrm{V_l}}$ and $k_{\mathrm{V_t}}$ are the wavenumbers given by $k_{\mathrm{V_l}}(\omega) = \omega / c_{\mathrm{V_l}}(\omega)$ and $k_{\mathrm{V_t}}(\omega) = \omega / c_{\mathrm{V_t}}(\omega)$ where $c_{\mathrm{V_l}}(\omega) = \sqrt{(\lambda(\omega) + 2\mu(\omega))/\rho_{\mathrm{V}}}$ is the sound velocity of the longitudinal waves, and $c_{\mathrm{V_t}}(\omega) = \sqrt{\mu(\omega)/\rho_{\mathrm{V}}}$ is the sound velocity of the transverse waves, being ρ_{V} is the mass density of the viscoelastic solid, $\lambda(\omega)$ and $\mu(\omega)$ the Lamé coefficients associated to the material, given by (5), and

$$\boldsymbol{d}_{\mathrm{l}}^- = \begin{pmatrix} -\cos\theta_{\mathrm{V_l}} \\ \sin\theta_{\mathrm{V_l}} \end{pmatrix}, \boldsymbol{d}_{\mathrm{l}}^+ = \begin{pmatrix} \cos\theta_{\mathrm{V_l}} \\ \sin\theta_{\mathrm{V_l}} \end{pmatrix},$$

$$\boldsymbol{d}_{\mathrm{t}}^- = \begin{pmatrix} -\cos\theta_{\mathrm{V_t}} \\ \sin\theta_{\mathrm{V_t}} \end{pmatrix}, \boldsymbol{d}_{\mathrm{t}}^+ = \begin{pmatrix} \cos\theta_{\mathrm{V_t}} \\ \sin\theta_{\mathrm{V_t}} \end{pmatrix},$$

and $\left(\boldsymbol{d}_{\mathrm{t}}^-\right)^{\perp}$ and $\left(\boldsymbol{d}_{\mathrm{t}}^+\right)^{\perp}$ are unit perpendicular vectors to $\boldsymbol{d}_{\mathrm{t}}^-$ and $\boldsymbol{d}_{\mathrm{t}}^+$, respectively.

Now, it is necessary to solve the propagation problem (6) to compute the amplitudes which determine the plane waves on each medium. The standard Transfer Matrix Method (TMM) [2, Chapter 11] is used to solve the linear system

$$\boldsymbol{A}(E', E'')\boldsymbol{y} = \boldsymbol{b}, \tag{16}$$

where $\boldsymbol{A}$ is a square matrix whose coefficients are explicitly written in terms of the real and the imaginary part of the Young's modulus (E' and E'', respectively), $\boldsymbol{y} = (A_{\mathrm{F}}, A_{\mathrm{B}}, B_{\mathrm{B}}, A_{\mathrm{V_l}}, B_{\mathrm{V_l}}, A_{\mathrm{V_t}}, B_{\mathrm{V_t}})^t$ is the unknown vector, formed by the amplitudes of the plane waves in each medium, and $\boldsymbol{b} = (B_{\mathrm{F}}, 0, 0, 0, 0, 0)^t$, where B_{F} is the amplitude of the incident wave in the front fluid propagating through the other media, which has been assumed known.

Once the system (16) is solved, by using the solutions $A_{\mathrm{F}}, B_{\mathrm{F}}, A_{\mathrm{B}}, B_{\mathrm{B}}, A_{\mathrm{V_l}}, B_{\mathrm{V_l}}, A_{\mathrm{V_t}}, B_{\mathrm{V_t}}$ is straightforward to compute the reflection and the transmission coefficients taking into account

$$P_{\mathrm{in}} = -i\omega Z_{\mathrm{F}} A_1, \qquad P_{\mathrm{rf}} = -i\omega Z_{\mathrm{F}} B_1, \qquad P_{\mathrm{tr}} = -i\omega Z_{\mathrm{F}} B_3.$$

Once the acoustic mathematical models have been described, the multilayer problem under study has been explained, and the acoustic quantities have been defined, the following section focuses on the numerical solution of the inverse problem used to characterize the viscoelastic material.

4. Data-driven characterization of a viscoelastic solid using a gradient-based optimization

The only known data of the polymer tile are its dimensions, mass density, and the frequency responses of the insertion loss and the fractional power dissipation. Since to get the acoustic characterization of an absorbing tile by using a viscoelastic model, it is necessary to know its Poisson's ratio and its Young's modulus, the purpose of this inverse problem is to find the values of the real and the imaginary parts of Young's modulus, E' and E'', respectively, which provide a frequency response as close as possible to that provided by experimental measurements. Throughout the rest of this work, Poisson's ratio is supposed to be constant and known according to the experimental data available in the literature (see [35]). Moreover, a potential change in Poisson's ratio does not affect the frequency response of the viscoelastic wavenumber $k_{\mathrm{V_l}}(\omega)$ since it could be balanced rescaling by a constant factor on the real and imaginary part of the complex-valued Young's modulus.

4.1. Selection of the primal unknowns

The characterization of the viscoelastic layer requires the solution of an inverse problem which fits the experimental data and the properties of the constitutive laws. Two different selections of primal unknowns are considered to write the parametric and data-driven constitutive laws of the viscoelastic material.

4.1.1. Parametric inverse problem

First, a parametric fitting was performed to characterize the constitutive laws of the viscoelastic material. The real and imaginary parts of the Young's modulus are the primal unknowns of the inverse problem and follow the Kelvin-Voigt model [10,18,33]. In this case, its real part is constant, and its imaginary part depends linearly on the frequency, i.e., the Young's modulus of a viscoelastic material [35] can be written as $E = E' - i\omega E''$, where E' and E'' are assumed constant.

Throughout this work, the experimental values of the insertion loss and the fractional power dissipation are taken into account. The same data-driven approach has been applied to both levels. If $\mathrm{L}_j^{\mathrm{exp}}$ denotes the experimental values obtained by measuring the level under study, for $j = 1, \ldots, N_{\mathrm{L}}$, being N_{L} the number of considered frequencies, and $\widehat{\mathrm{L}}(E', E'', \omega_j)$ is the computed numerical values of the level under consideration for a fixed angular frequency ω_j with $j = 1, \ldots, N_{\mathrm{L}}$, then the cost function is defined as

$$\Phi_{\mathrm{L}}(E', E'') = \frac{\sqrt{\sum_{j=1}^{N_{\mathrm{L}}} |\mathrm{L}_j^{\mathrm{exp}} - \widehat{\mathrm{L}}(E', E'', \omega_j)|^2}}{\sqrt{\sum_{j=1}^{N_{\mathrm{L}}} |\mathrm{L}_j^{\mathrm{exp}}|^2}}. \tag{17}$$

Hence, the parametric inverse problem is stated as follows: Find the values $E' \geq 0$ and $E'' \geq 0$, such that minimizes the difference between the experimental and the predicted numerical values, i.e.,

$$(E', E'') = \underset{\mathcal{E}', \mathcal{E}'' > 0}{\arg\min}\, \Phi_{\mathrm{L}}(\mathcal{E}', \mathcal{E}''), \tag{18}$$

where recall that the Kelvin-Voigt model is used, i.e. $E = E' - i\omega E''$. It is observed that if the primal unknowns are the real and the imaginary parts of the Young's modulus, then spurious oscillations appear in the solution of the inverse problem due to its ill-posedness. This issue is overcome by considering a new pair of unknowns depending on the wavenumber and the thickness of the viscoelastic layer.

4.1.2. Data-driven inverse problem

To mitigate partially the issues observed in the parametric model, now it is assumed that an arbitrary smooth frequency-dependent function governs the Young's modulus, this is, the real and the imaginary

parts of the Young's modulus are governed by an arbitrary function that depends on the angular frequency (see Definition 2.1). In this data-driven approach, the cost function is defined as

$$\Psi_{\mathrm{L}}(E', E'', \omega_j) = \frac{|\mathrm{L}_j^{\mathrm{exp}} - \widehat{\mathrm{L}}(E'_j, E''_j, \omega_j)|^2}{|\mathrm{L}_j^{\mathrm{exp}}|^2} \quad \text{for } j = 1, \dots, N_{\mathrm{L}}. \tag{19}$$

Notice that in this case, the real and the imaginary part of the Young's modulus $E_j = E'_j - iE''_j$, are different for each angular frequency ω_j. Then, the data-driven inverse as follows: For each $j = 1, \dots, N_{\mathrm{L}}$, find the values $E'_j \geq 0$ and $E''_j \geq 0$ such that minimize the difference between the experimental and the predicted numerical values, i.e.,

$$(E'_j, E''_j) = \underset{\mathcal{E}'_j, \mathcal{E}''_j > 0}{\arg\min}\, \Psi_{\mathrm{L}}(\mathcal{E}'_j, \mathcal{E}''_j, \omega_j) \quad \text{for } j = 1, \dots, N_{\mathrm{L}}. \tag{20}$$

As in the parametric approach, a direct inspection of the solution to this minimization problem shows that the inverse problem is ill-posed: the solutions of the inverse problem associated with two close angular frequencies ω_j and $\omega_j + 1$ lead to very different values when the pairs (E'_j, E''_j) and (E'_{j+1}, E''_{j+1}) are compared, which produces spurious oscillations the frequency response of Young's modulus (see Section 5.4 for more details).

Hence, new primal unknowns should be chosen to overcome this issue and get smoother frequency responses for Young's modulus. A proper choice of the new primal unknowns must remedy the oscillatory behaviour, which comes from the computation of the reflected and the transmitted pressure fields. As can be observed in Equations (14) and (15), the transmission and the reflection coefficients of a plane wave propagation problem are involved in these integral expressions, and both coefficients are computed by using the linear system (16). In this linear system, there exists an exponential dependence of the coefficients with respect to the value of the Young's modulus. This fact also implies that the numerical results computed from (20) are highly dependent on the initial guess: small changes in the initial guess lead to pretty different numerical results. To mitigate this situation, instead of using the unknowns E' and E'' in the minimization procedure (20), a novel pair of unknowns, $\delta = \mathrm{Re}(k_{\mathrm{V_l}})l$ and $M = e^{\mathrm{Im}(k_{\mathrm{V_l}})l}$, has been considered, where recall that $k_{\mathrm{V_l}}$ is the wavenumber of the longitudinal waves in the viscoelastic medium, and l is the thickness of the viscoelastic layer. Consequently, the exponential dependence of the transmission and reflection coefficients with respect to the unknowns is avoided. The exponential terms depending on the Young's modulus in the linear system (16) can be rewritten in terms of δ and M, and the new linear system results

$$\boldsymbol{A}(M, \delta)\boldsymbol{y} = \boldsymbol{b}, \tag{21}$$

where abusing the notation, the coefficients of matrix $\boldsymbol{A}$ in (21) must be read as functions M and δ.

Then, the computation of the reflection and the transmission coefficients using M and δ allows for avoiding those spurious oscillations. Once these two coefficients are calculated for each fixed angular frequency and angle of incidence, the transmitted and the reflected fields are obtained using expressions (14) and (15). If the same notation L is used for the level function considered in the inverse problem, the cost function is defined in terms of M and δ as follows:

$$\Upsilon_{\mathrm{L}}(M, \delta, \omega_j) = \frac{|\mathrm{L}_j^{\mathrm{exp}} - \widehat{\mathrm{L}}(M, \delta, \omega_j)|^2}{|\mathrm{L}_j^{\mathrm{exp}}|^2} \quad \text{for } j = 1, \dots, N_{\mathrm{L}}, \tag{22}$$

and hence the data-driven inverse problem is given by: Find the values $M_j \geq 0$ and $\delta_j \geq 0$ such that minimize the difference between the experimental and the numerical values, i.e.,

$$(M_j, \delta_j) = \underset{\mathcal{M}, \gamma > 0}{\arg\min}\, \Upsilon_{\mathrm{L}}(\mathcal{M}, \gamma, \omega_j) \quad \text{for } j = 1, \dots, N_{\mathrm{L}}, \tag{23}$$

where M_j and δ_j are the novel unknowns given by $M_j = e^{\mathrm{Im}(k_{\mathrm{V_l}j})l}$ and $\delta_j = \mathrm{Re}(k_{\mathrm{V_l}j})l$.

In this proposed data-driven approach, a trust-region reflective algorithm (see [11]) has been used to solve the minimization problem (23). This algorithm is based on the interior-reflective Newton method (see [12] and [13] for more details) and requires the computation of the gradient of the function to be minimized.

4.2. Gradient computations

Taking into account the expression of the cost function in (23), its gradient with respect to $\boldsymbol{p} = (M, \delta)^t$ is given by

$$\partial_{\boldsymbol{p}} \Upsilon_{\mathrm{L}}(\boldsymbol{p}, \omega) = \frac{2\,\mathrm{sign}\left(\mathrm{L}^{\mathrm{exp}} - \widehat{\mathrm{L}}(\boldsymbol{p}, \omega)\right) |\mathrm{L}^{\mathrm{exp}} - \widehat{\mathrm{L}}(\boldsymbol{p}, \omega)|}{|\mathrm{L}^{\mathrm{exp}}|^2} \partial_{\boldsymbol{p}} \widehat{\mathrm{L}}(\boldsymbol{p}, \omega),$$

where the computation of $\partial_{\boldsymbol{p}} \widehat{\mathrm{L}}$ is detailed below to consider the differences when the level L is IL or FPD. If the pressure field $P_{\mathrm{rf}}(\boldsymbol{x})$ and $P_{\mathrm{tr}}(\boldsymbol{x})$ are formally written in terms of response functions to write the explicit dependency of those fields with respect to the primal variables $\boldsymbol{p}$ and ω, then

$$P_{\mathrm{tr}}(\boldsymbol{x}) = \widehat{P}_{\mathrm{tr}}(\boldsymbol{p}, \omega, \boldsymbol{x}), \qquad P_{\mathrm{rf}}(\boldsymbol{x}) = \widehat{P}_{\mathrm{rf}}(\boldsymbol{p}, \omega, \boldsymbol{x}).$$

Taking into account the definition of the insertion loss (9) and the fractional power dissipation (10), these levels can be read as dependent expressions on $\boldsymbol{p}$ and their respective gradients are given by

$$\partial_{\boldsymbol{p}} \mathrm{IL} = \frac{-10}{|\widehat{P}_{\mathrm{tr}}|^2 \log 10} \partial_{\boldsymbol{p}} (|\widehat{P}_{\mathrm{tr}}|^2),$$

$$\partial_{\boldsymbol{p}} \mathrm{FPD} = \frac{-2}{|\widehat{P}_{\mathrm{inc}}|^2} \left[\partial_{\boldsymbol{p}} (|\widehat{P}_{\mathrm{tr}}|^2) + \partial_{\boldsymbol{p}} (|\widehat{P}_{\mathrm{rf}}|^2) \right],$$

where the gradient of the modulus of a complex-valued scalar field Q is computed in closed form as $\partial_{\boldsymbol{p}}(|Q|^2) = 2(\mathrm{Re}(Q)\mathrm{Re}\left(\partial_{\boldsymbol{p}} Q\right) + \mathrm{Im}(Q)\mathrm{Im}\left(\partial_{\boldsymbol{p}} Q\right))$, which is applied for $Q = \widehat{P}_{\mathrm{rf}}, \widehat{P}_{\mathrm{tr}}$ in the expressions above. Finally, taking into account (15) and (14), the computation of the gradient of the cost function requires the gradients of the response functions $\widehat{P}_{\mathrm{tr}}$ and $\widehat{P}_{\mathrm{tr}}$ as follows:

$$\partial_{\boldsymbol{p}} \widehat{P}_{\mathrm{rf}} = ik_{\mathrm{F}} \int_0^{\frac{\pi}{2} - i\infty} S(\theta)(\partial_{\boldsymbol{p}} y_1) e^{ik_{\mathrm{F}} x_3 \cos\theta} \sin\theta \, \mathrm{d}\theta,$$

$$\partial_{\boldsymbol{p}} \widehat{P}_{\mathrm{tr}} = ik_{\mathrm{F}} \int_0^{\frac{\pi}{2} - i\infty} S(\theta)(\partial_{\boldsymbol{p}} y_3) e^{ik_{\mathrm{F}} x_3 \cos\theta} \sin\theta \, \mathrm{d}\theta,$$

where recall $S(\theta)$ is the plane wave spectrum of the truncated parametric source, given by (12), y_1 and y_3 are the first and the third components of the vector $\boldsymbol{y}$, which denotes the amplitudes of reflected and transmitted waves, respectively, obtained from the resolution of the linear system (21) written in terms of $\boldsymbol{p} = (M, \delta)^t$.

The computation of the gradient of the reflected and transmitted plane waves computed in (21) for a fixed angular frequency and a given angle of incidence is described in what follows. Let $\boldsymbol{y}$ be the vector solution of the linear system (21), and $\boldsymbol{p} = (M, \delta)^t$ the primal unknowns used in the data-driven inverse problem. If the dependency of the vector solution $\boldsymbol{y}$ with respect to $\boldsymbol{p}$ is written explicitly, the equation of state can be written as $\boldsymbol{A}(\boldsymbol{p})\boldsymbol{y}(\boldsymbol{p}) = \boldsymbol{b}(\boldsymbol{p})$, where $\boldsymbol{A}$ and $\boldsymbol{b}$ are the matrix and the right-hand side of the linear system in (21). Consequently, computing the partial derivatives with respect to $\boldsymbol{p}$, it holds

$$(\partial_{\boldsymbol{p}} \boldsymbol{A})\boldsymbol{y} + \boldsymbol{A}\partial_{\boldsymbol{p}} \boldsymbol{y} = \partial_{\boldsymbol{p}} \boldsymbol{b} \quad \Rightarrow \quad \partial_{\boldsymbol{p}} \boldsymbol{y} = \boldsymbol{A}^{-1} \left(\partial_{\boldsymbol{p}} \boldsymbol{b} - (\partial_{\boldsymbol{p}} \boldsymbol{A})\boldsymbol{y}\right). \tag{24}$$

It is straightforward to check that only two linear systems with matrix $\boldsymbol{A}$ (for each partial derivative with respect to M and δ) are required to compute the partial derivatives of $\boldsymbol{y}$.

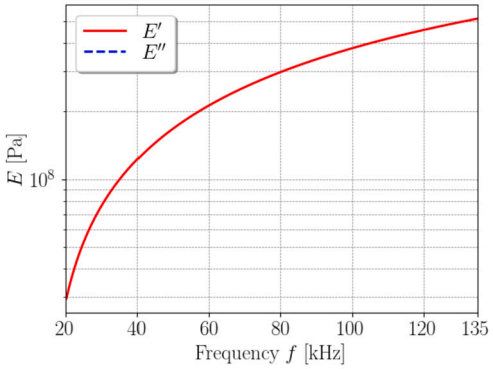

Fig. 2. Values of the real and the imaginary parts (solid blue and dashed red line, respectively), which have been chosen as the Young's modulus of the manufactured material.

5. Numerical results

Once the different constitutive laws over the Young's modulus have been described, and the gradient computations associated with the inverse problems are analysed, this section focuses on the numerical simulations of the inverse problem. First, code validation has been performed to ensure the robustness of the methodology. For this purpose, some manufactured data have been created. Then, the available experimental data are described, which have been used to perform parametric and data-driven simulations. All the numerical results in this section consider an end-fire array as an acoustic source with a non-planar directivity pattern. In addition, the mass density of the water in terms of the hydrostatic pressure and the temperature, the standard IAPWS95 is used, *International Association for the Properties of Water and Steam, Formulation 1995*, (see [26] and [24] for more details). Also, it is supposed that a response function gives the sound speed depending on the hydrostatic pressure and the temperature following [6]. According to [7] and [29], the attenuation coefficient of the water results

$$\alpha = 0.11 \times 10^{-12} \frac{\ln 10}{(2\pi)^2} = 6.42 \times 10^{-16}\, \mathrm{s}^2/\mathrm{m}.$$

Following [23], the length of the parametric end-fire array is $h = 1.88$ m and the constant $Q_0 = 1$ Pa.

5.1. Code validation

Some numerical simulations with manufactured data have been performed to validate the code. Since a viscoelastic material is manufactured, it is necessary to consider the values of the Young's modulus and Poisson's ratio, which describe the viscoelastic behaviour of the material as well as the thickness and mass density. In this case, the mass density $\rho_{\mathrm{V}} = 2100$ kg/m^3, the thickness $\mathrm{l} = 0.05$ m, and the Poisson's ratio $\nu = 0.48$. It is supposed that an arbitrary frequency-dependent function governs the Young's modulus (see Fig. 2), that is, $E_j = E'_j - iE''_j$ for $j = 1, \ldots, N_{\mathrm{L}}$, where N_{L} is the number of considered frequencies.

By using the values of the Young's modulus shown in Fig. 2, and taking into account the non-planar directivity pattern of the acoustic source described in (12), the experimental data for insertion loss and fractional power dissipation can be computed by using the definitions appearing in Section 2.3. The resulting manufactured data are shown in Fig. 3. The validation of the code is performed considering the minimization problem with the unknowns $\delta = \mathrm{Re}(k_{\mathrm{V_l}})l$ and $M = e^{\mathrm{Im}(k_{\mathrm{V_l}})l}$ (see Section 4.1.2 for more details) and working with the cost function associated with each level individually. The initial guess for the trust-region reflective algorithm has been computed to minimize the cost function (23) in a two-dimensional 10×10 log-scaled Cartesian (M, δ)-discrete grid with bounds $[10^{-2}, 10^2] \times [1, 10^2]$ for the higher angular frequency. With this strategy, the guess value of the Young's modulus is $E = 5.09 \times 10^8 - i1.84 \times 10^7$ Pa. The results of the inverse problem associated with the insertion loss and the fractional power dissipation are shown in Figs. 4 and 5, respectively. In the left plots, the manufactured data, with a solid blue line, and the predicted numerical values, with a dashed red line, of each level are plotted with respect to the frequency. The real and the imaginary parts of the Young's modulus are plotted in the right plots. The inverse problem solved to obtain the predicted values is given by (23), and the relative errors are $\epsilon_{\mathrm{IL}} = 4.21 \times 10^{-11}\%$, and $\epsilon_{\mathrm{FPD}} = 4.65 \times 10^{-10}\%$.

Table 1
Real and imaginary parts of the Young's modulus, and relative errors in every single inverse problem, assuming that the Young's modulus is a linear function of the frequency.

	IL data	FPD data
E' [Pa]	1.2328×10^9	7.5646×10^7
E'' [Pa]	5.5908×10^3	114.9757
ϵ_{IL}	3.14%	238.53%
ϵ_{FPD}	49.63%	2.86%

Although this problem is ill-posed (due to the limited and real-valued experimental data used in the cost function definition), the errors obtained in the solution of each inverse problem are negligible. As can be observed in the right plots of Figs. 4 and 5, the obtained real and imaginary parts of the Young's modulus have similar behaviour to the manufactured ones given in Fig. 2 and are smooth enough, which validates the proposed data-driven approach.

To illustrate the robustness of the proposed methodology with respect to the selected initial guess (used in the frequency-by-frequency non-linear optimization), a variety of initial guesses has been considered in 10×10 grid around the exact value. The predicted frequency responses for the quantities of interest IL and FPD, and also the real and imaginary parts of the Young's modulus are plotted in Fig. 6. To show a sharp estimation of the variability of this frequency response function, functional medians of these sets of functions have been computed. These functional medians correspond to curves that can be obtained for a particular initial guess. On the contrary, the computation of the pointwise-mean curve would lead to a fictitious curve (see [38] for a detailed discussion), which does not represent any realization of the optimization procedure described in the sections above.

Additionally, the associated functional 95% confidence level bands using the modal depth have also been computed (see [15] for further details). These functional computations have been performed using a bootstrap procedure with 500 resamples, and the smoothing parameter for the bootstrap samples, which is settled as a proportion of the sample variance matrix, has been fixed to 0.1. For this purpose, the R package fda.usc [16] has been used in the implementation. The same statistical setting has been utilized throughout the rest of this work.

As can be observed in Figs. 7 and 8, despite slight changes in the initial guess are leading to different frequency response functions for the real and imaginary part of Young's modulus, such differences are almost negligible on the levels IL of FPD where the confidence bands are not appreciable (see the thin shaded grey regions in the plots of Fig. 6). This numerical dependency on the initial guess in the inverse problem is consistent with the cost function exhibiting multiple local minima and stagnation regions with similar values.

5.2. Experimental data

The material under consideration is the AptFlex SF5048 (see [1]). This material is an engineered polymer used in underwater acoustic applications. This viscoelastic tile has a known thickness, mass density, and IL and FPD frequency responses. In Fig. 9, the frequency response of this polymeric layer is shown in a frequency range between 20 and 135 kHz.

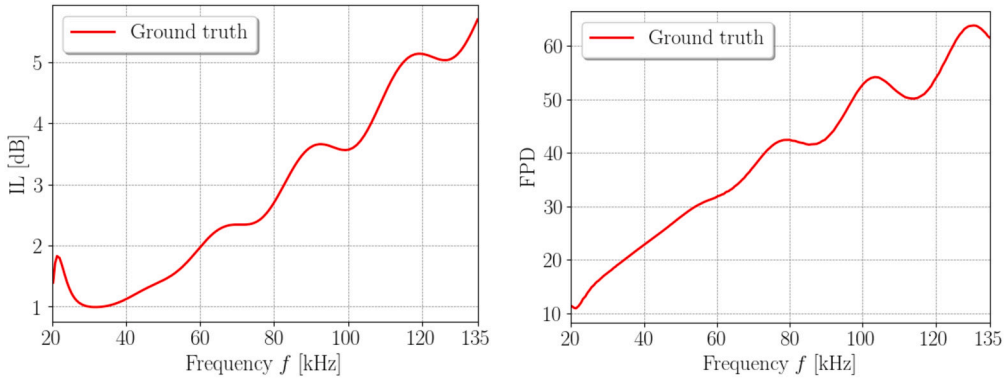

Fig. 3. Frequency response of a manufactured material with mass density $\rho_V = 2100$ kg/m^3, thickness $l = 0.05$ m, Poisson's ratio $\nu = 0.48$, and Young's modulus given in Fig. 2, for the insertion loss level (left) and fractional power dissipation (right).

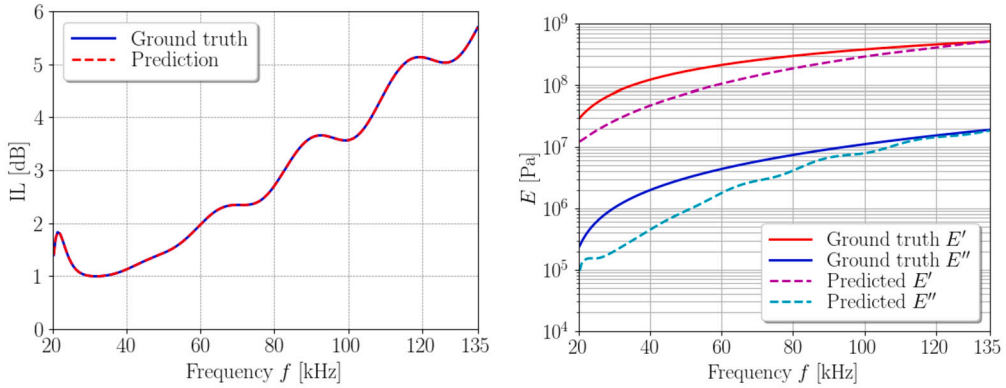

Fig. 4. Left: Manufactured (solid blue line) and predicted (dashed red line) values of the insertion loss level plotted with respect to the frequency. Right: Values of the real and imaginary parts of the Young's modulus (solid line: manufactured data, dashed line: predicted ones). The considered inverse problem is (23), where L =IL.

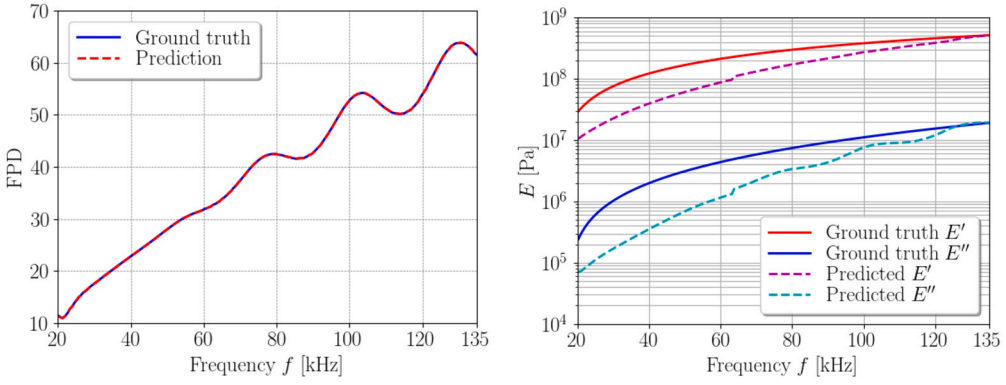

Fig. 5. Left: Manufactured (solid blue line) and predicted (dashed red line) values of the fractional power dissipation plotted with respect to the frequency. Right: Values of the real and imaginary parts of the Young's modulus (solid line: manufactured data, dashed line: predicted ones). The considered inverse problem is (23), where L =FPD.

To compute the data-driven characterization of AptFlex SF5048 by using a viscoelastic model, the Poisson's ratio is supposed to be known with the value $\nu = 0.48$, following the work [25], which is the generic value for polyurethane elastomers. Besides, following the technical specifications provided by the supplier of the material Aptflex SF5048 (see [1]), the polymer mass density is $\rho_V = 2100\,\mathrm{kg/m^3}$, and the thickness $l = 0.05\,\mathrm{m}$.

5.3. Characterization with a parametric model

In this section, the numerical simulations are performed with the available experimental data, shown in Fig. 9, using the Kelvin-Voigt model and considering a plane wave with an oblique incidence angle as the acoustic source. More precisely, following [35], it was considered that the Young's modulus of the polymer tile could be written as $E = E' - i\omega E''$ where E' and E'' are assumed constant. This numerical solution of the parametric problem is performed by using an exhaustive nested search global optimization algorithm. Since the range for the real and the imaginary parts of the Young's modulus is extensive, an optimization strategy based on a brute force searching algorithm has been implemented on log-scaled Cartesian grids. Although this algorithmic procedure is computationally costly, this strategy allows us to find the global minimum of a function of two variables in successive refined

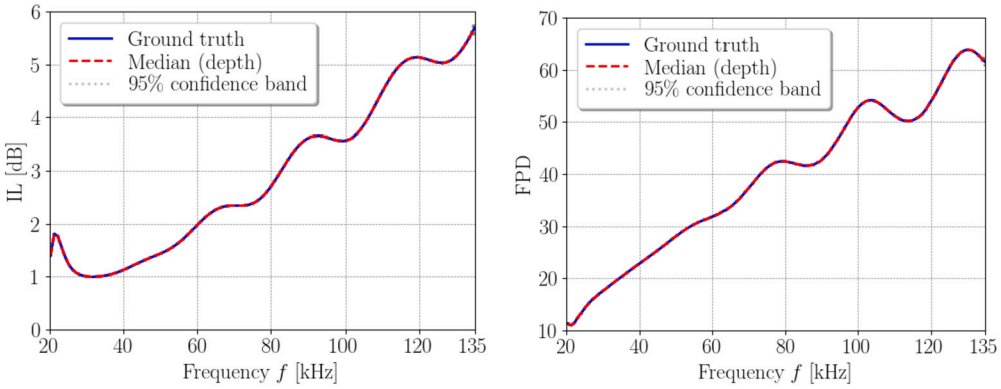

Fig. 6. Manufactured values (solid blue line) of the insertion loss (left) and fractional power dissipation (right) plotted with respect to the frequency for the solution of the inverse problem associated with each level. Shaded grey lines represent the 95% confidence level bands computed using the functional medians of sets of frequency responses obtained using different initial guesses in a grid. The dashed red line corresponds with the depth median. The inverse problem is given by (23), with L = IL and FPD.

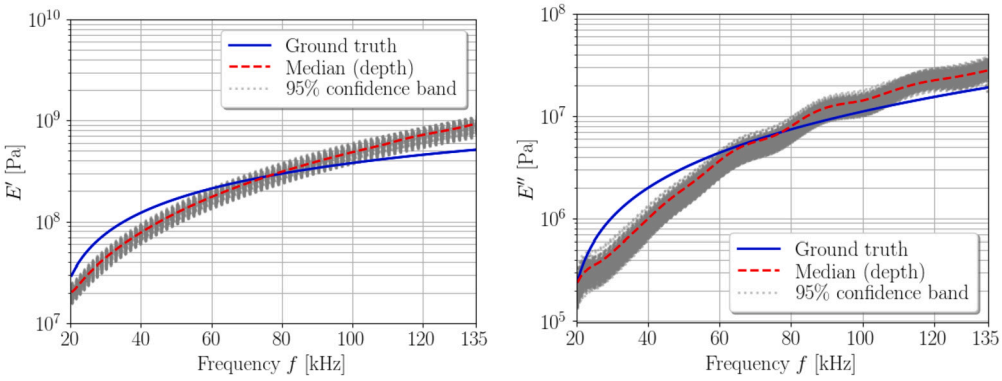

Fig. 7. Manufactured values (solid blue line) of the real (left plot) and imaginary (right plot) parts of the Young's modulus for the IL inverse problem. Shaded grey lines represent the 95% confidence level bands computed using the functional medians of sets of frequency responses obtained using different initial guesses in a grid. The dashed red line corresponds with the depth median. The inverse problem (23) uses IL data.

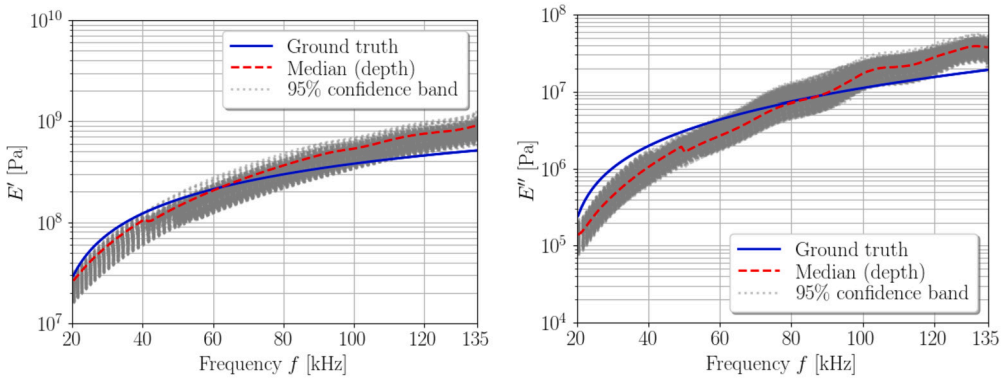

Fig. 8. Manufactured values (solid blue line) of the real (left plot) and imaginary (right plot) parts of the Young's modulus for the FPD fitting. Shaded grey lines represent the 95% confidence level bands computed using the functional medians of sets of frequency responses obtained using different initial guesses in a grid. The dashed red line corresponds with the depth median. The inverse problem (23) uses FPD data.

two-dimensional Cartesian discrete grids, and hence avoiding potential local minima in the parametric cost function.

A log-scaled grid of 300×300 of points is considered with bounds for $E' \in [10^4, 10^{10}]$ and $E'' \in [10^2, 10^8]$. The cost function values at each grid point are computed, and the first approximated value is the grid location (E'_1, E''_1) where the global minimum is reached. For performing a new iteration, a new log-scaled grid is centred in the previous iterant with bounds $E' \in [E'_1 \times 10^{-0.5}, E'_1 \times 10^{0.5}]$ and $E'' \in [E''_1 \times 10^{-0.5}, E''_1 \times 10^{0.5}]$. This iterative process stops once two consecutive iterants are closer than a tolerance of 10^{-2}. In the present case, only two iterations were required to hold the stopping criterion with the available experimental data described above.

The comparison between the experimental data and the predicted ones is shown in Fig. 10 (left: insertion loss; right: fractional power dissipation). The fitting for IL and FPD shows good agreement. Table 1 shows the real and the imaginary parts of the Young's modulus obtained

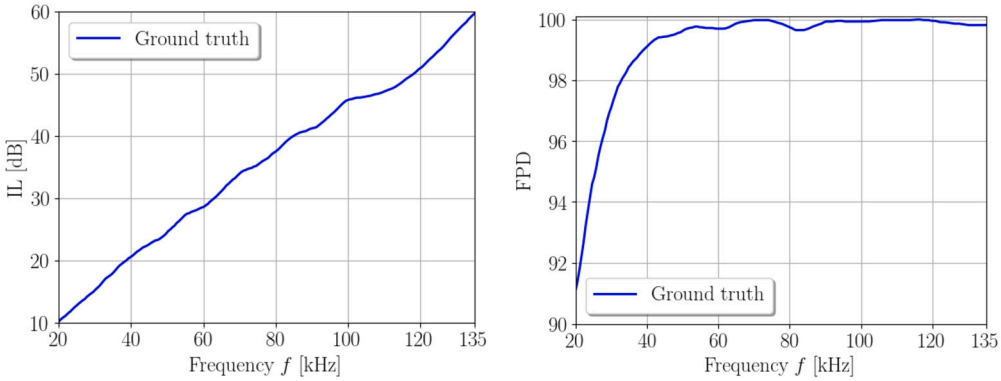

Fig. 9. Experimental values of the frequency response of the AptFlex SF5048 for the insertion loss (left) and the fractional power dissipation (right).

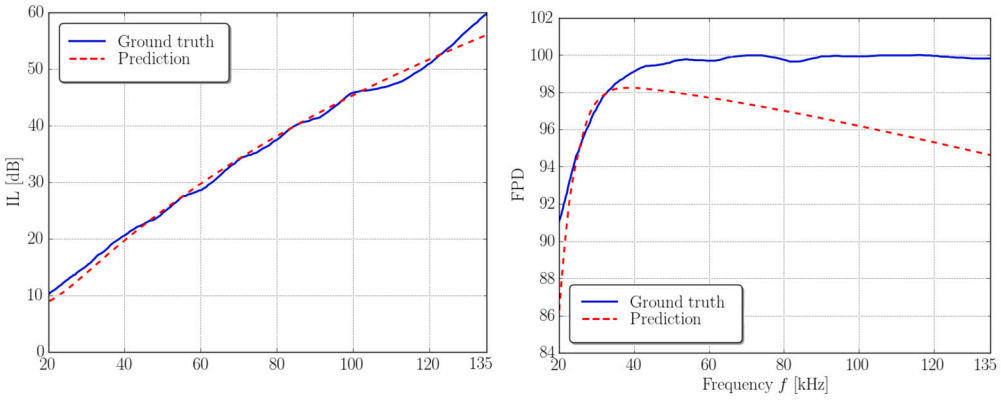

Fig. 10. Experimental (solid blue line) and predicted (dashed red line) values of the insertion loss (left) and the fractional power dissipation (right) plotted with respect to the frequency.

with the minimization problem (18), and the relative error computed using (17). The IL and FPD curves in Fig. 10 indicate a partial agreement between the parametric model and the experimental data. Even though the relative error obtained for the (E', E'')-values computed for each level (IL and FDP) are lower than 5% (see the shaded grey cells in Table 1), the calculated values for the inverse problem involving the IL fitting or the FPD fitting are drastically different (differences of two orders of magnitude for E'). These notorious differences could be read as a symptom that the parametric Kelvin-Voigt model is unsuitable for modelling the entire frequency range included in the experimental data. However, it should be noted that an overall good agreement is achieved for the IL and FPD data below 40 kHz.

5.4. Characterization with the data-driven approach

As explained in Section 4, the data-driven approach computes (M_j, δ_j) independently for each fixed frequency ω_j for $j = 1, \dots, N_L$ in the inverse problem (23). The inverse problem associated with each level (IL or FPD) has been solved separately using this algorithm. As in previous simulations, the frequency sweeping procedure has been solved from higher to lower frequencies.

The numerical results for the insertion loss and the fractional power dissipation are shown in Figs. 11 and 12. In the left plots, the experimental data in a solid blue line and the predicted ones in a dashed red line are plotted with respect to the frequency, and in the right plots, the real and the imaginary parts of the Young's modulus (in solid blue line and dashed red line, respectively) are shown. The relative errors of single inverse problems computed by using (22) are $\varepsilon_{\text{IL}} = 2.156 \times 10^{-6}\%$, and $\varepsilon_{\text{FPD}} = 0.188\%$ (see highlighted grey cells in Table 2).

Using the frequency response of the Young's modulus computed from the IL data, it is possible to calculate the error reached using FPD data and vice versa. Table 2 also shows these relative errors in the off-diagonal cells. As can be observed from the errors reported in Table 2, the characterization of Young's modulus based on IL data provides overall accurate results (errors smaller than 10% both for IL and FPD data). In both cases, despite a data-driven approach is being used without prescribing any parametric dependency, the frequency response of the real and the imaginary parts of the Young's modulus show smooth trends (see right plots of Figs. 11 and 12). However, the predicted values of E' and E'' still behaviours in the same range of values (E' around 10^8 Pa and E'' around 10^7 Pa). Finally, it should be noted that the frequency response computed from the FPD data presents a different trend below 40 kHz (a feature already observed with the parametric model). With the aim of overcoming this duplicity on the computed frequency response functions, a joint data-driven inverse problem has been used, combining IL and FPD data in the same cost function. In this manner, the inverse problem consists in finding the values $M_j > 0$ and $\delta_j > 0$, such that minimizes the difference between the experimental and the numerical values, i.e., for $j = 1, \dots, N_L$

Table 2
Relative errors in the single inverse problem, using the novel primal unknowns M and δ. The minimization problem under consideration is (23). The relative errors are computed by using (22), where L is IL and FPD, respectively.

	IL data	FPD data
ε_{IL}	$2.156 \times 10^{-6}\%$	32.61%
ε_{FPD}	8.60%	0.188%

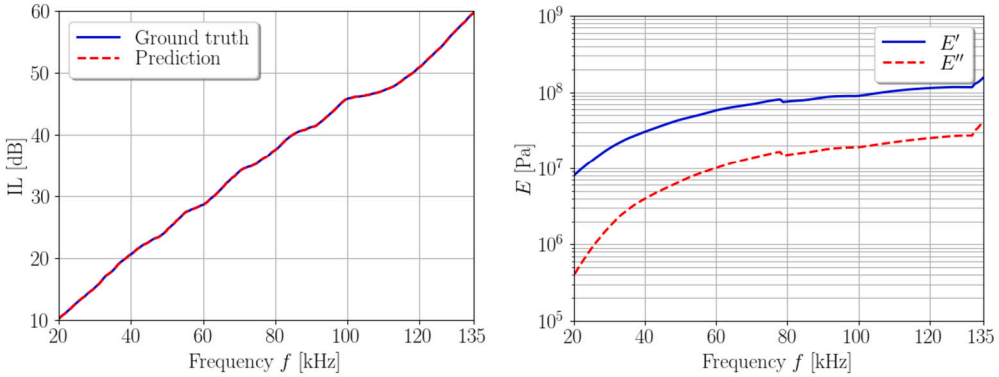

Fig. 11. Left: Experimental (solid blue line) and predicted (dashed red line) values of the insertion loss level plotted with respect to the frequency. Right: Values of the real (solid blue line) and imaginary part (dashed red line) of the Young's modulus. The inverse problem under consideration is (23), where L =IL. The relative error is $\varepsilon_{\text{IL}} = 2.156 \times 10^{-6}\%$.

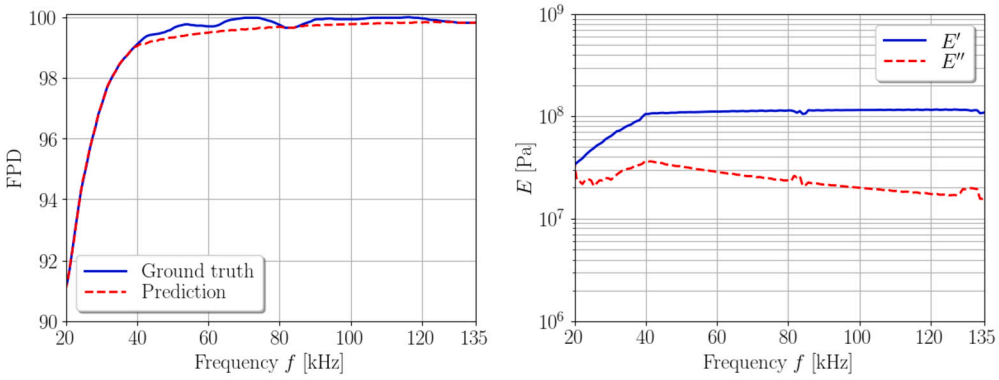

Fig. 12. Left: Experimental (solid blue line) and predicted (dashed red line) values of the fractional power dissipation plotted with respect to the frequency. Right: Values of the real (solid blue line) and imaginary part (dashed red line) of the Young's modulus. The considered inverse problem is (23) where L =FPD. The relative error is $\varepsilon_{\text{FPD}} = 0.188\%$.

$$(M_j, \delta_j) = \underset{\mathcal{M},\gamma>0}{\arg\min} \left(\Upsilon_{\text{IL}}(\mathcal{M}, \gamma, \omega_j) + \Upsilon_{\text{FPD}}(\mathcal{M}, \gamma, \omega_j) \right), \tag{25}$$

where Υ_{L} with $\text{L} = \text{IL}, \text{FPD}$ is given by (22), and M_j and δ_j are the novel unknowns given by $M_j = e^{\text{Im}(k_{\text{V}_1}(\omega_j))l}$ and $\delta_j = \text{Re}(k_{\text{V}_1}(\omega_j))l$. The comparison between the experimental data and the numerical predictions ones is shown in the top left, top right, and bottom left plots of Fig. 13 for the insertion loss and the fractional power dissipation, respectively. In the bottom plot, the real and the imaginary parts of the Young's modulus are plotted. The relative errors computed by using (25) are $\varepsilon_{\text{IL}} = 1.75 \times 10^{-6}\%$ and $\varepsilon_{\text{FPD}} = 3.35\%$. Once again, the computed frequency response for Young's modulus is quantitatively similar to those calculated only with IL data (comparing the right plots in Fig. 11 and the bottom plot in Fig. 13). However, when the joint data-driven problem is solved, the errors are decreased to less than 3%. Finally, it should be remarked that even in this case, the main differences between the experimental data and the predicted numerical values are located in the FPD data below 40 kHz.

Finally, a variety of initial guesses has been considered to illustrate the robustness of the method with respect to the selection of the initial guess value. In this case, a 10×10 log-scaled Cartesian grid has been used around the initial guess used above in the joint inverse problem for the highest frequency. The predicted values for IL and FPD and the real and imaginary parts of the Young's modulus are plotted in Figs. 14 and 15, respectively. Additionally, the associated functional 95% confidence level bands using the modal depth have also been computed. As can be observed in Figs. 14 and 15, minor changes in the initial guess lead to moderately different values on the Young's modulus frequency response affecting the predicted IL or FPD values only at higher frequencies.

Once the proposed data-driven algorithm computes subsequent frequencies (sweeping from higher to lower frequencies), a regularized trend is reached, the frequency response of the Young's modulus becomes smooth, and the IL and FPD confidence bands have a significantly reduced width. These numerical results are consistent with the fact that even the joint inverse problem is ill-posed since the cost function exhibits multiple local minima due to the limited amount of experimental data used for each fixed frequency: only two real-valued data (IL and FPD data) at each frequency value.

6. Conclusions

In the present work, a viscoelastic material has been numerically characterized by using the frequency response of the insertion loss and the fractional power dissipation. The main purpose of this work is to use a data-driven methodology to describe the mechanical behaviour of a homogeneous isotropic viscoelastic material. Then, a data-driven approach was considered to determine an arbitrary frequency response of the material under study. The proposed methodology avoids the choice of a parametric model in the constitutive law of the viscoelastic material. All the numerical predictions of those frequency responses are based on solving an inverse problem, which minimizes the distance between the experimental data and the numerical values.

A multilayer medium formed by the viscoelastic material, surrounded by a compressible fluid (water), is studied to reproduce the laboratory setting used to measure the experimental IL and FPD data. For this purpose, the mathematical models of dissipative compressible

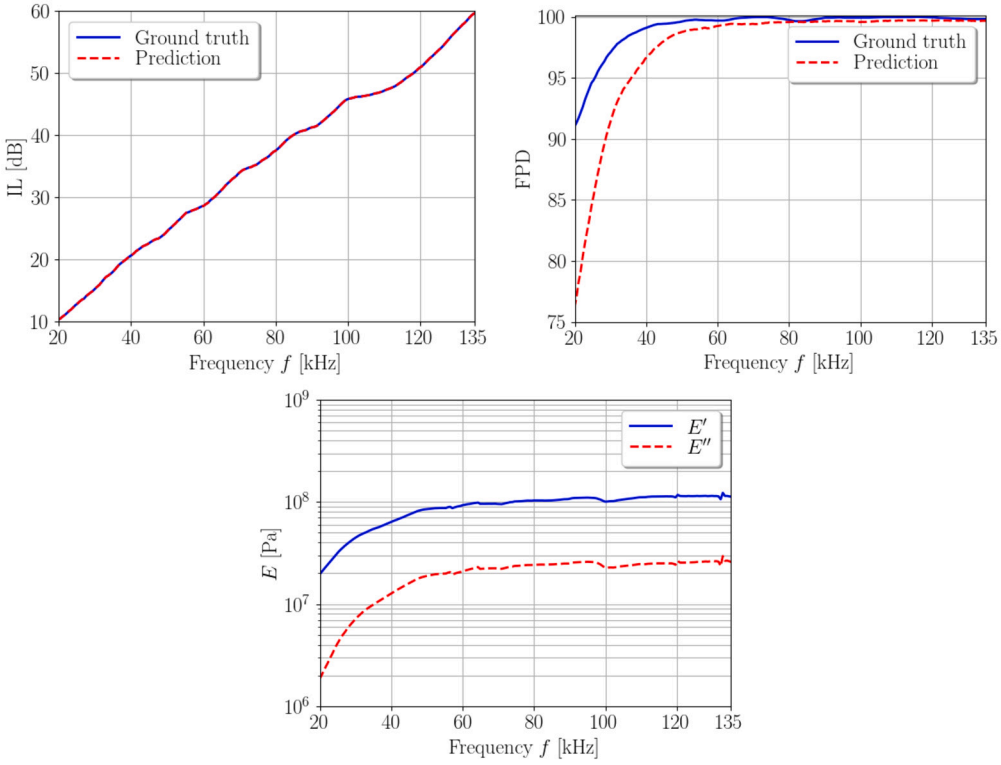

Fig. 13. Experimental (solid blue line) and predicted (dashed red line) values of the insertion loss (top left) and fractional power dissipation (top right) plotted with respect to the frequency for the joint inverse problem. Bottom: Values of the real (solid blue line) and imaginary part (dashed red line) of the Young's modulus.

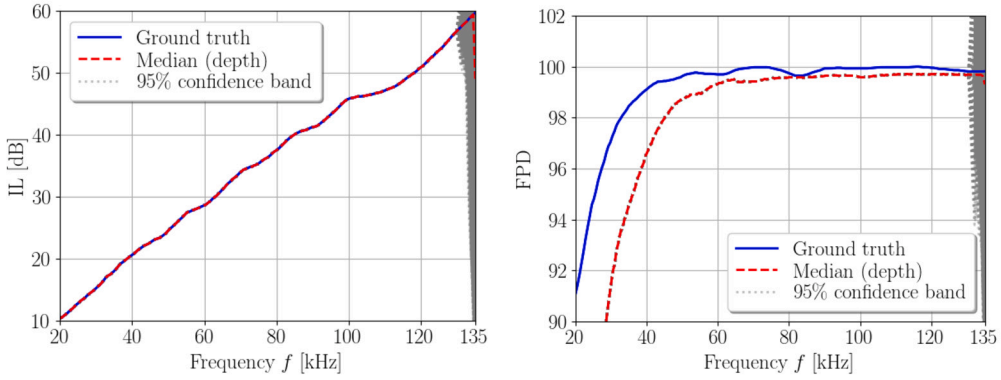

Fig. 14. Experimental values (solid blue line) of the insertion loss (left) and fractional power dissipation (right) plotted with respect to the frequency for the joint inverse problem. Shaded grey lines represent the 95% confidence level bands computed by using the functional medians of sets of predicted frequency responses, which are obtained by using different initial guesses in a grid. The dashed red line corresponds with the depth median.

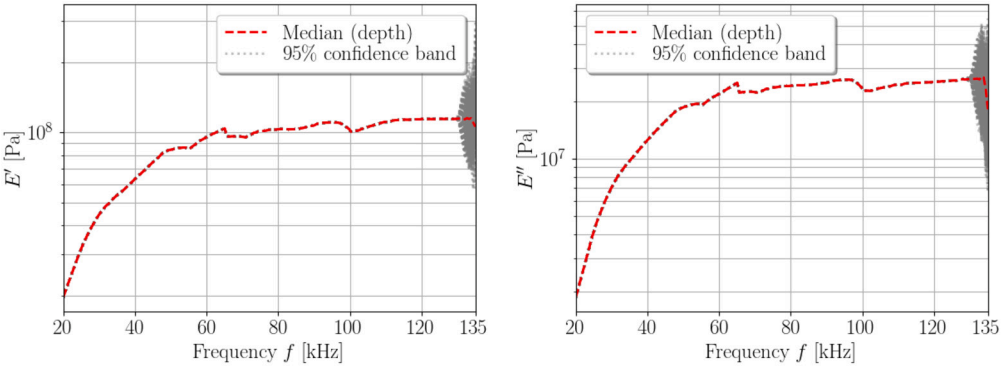

Fig. 15. Results for the real (left plot) and imaginary (right plot) parts of the Young's modulus. Shaded grey lines represent the 95% confidence level bands computed using the functional medians of sets of predicted frequency responses, which are obtained using different initial guesses in a grid. The dashed red line corresponds with the depth median.

fluids and viscoelastic solids are introduced. Then, the coupled mechanical problem and the acoustic quantities of interest for this problem have been described. Then, the direct problem of time-harmonic wave propagation in the multilayer medium was studied. Since the available experimental data are measured with an equipment setup where the acoustic source is a parametric array with a non-planar directivity pattern, the incident, reflected, and transmitted fields have been described using an integral representation. These integrals involve a non-constant plane wave spectrum and the reflection and transmission coefficients for a specific angle of incidence in a plane wave framework. The computation of these two coefficients was also detailed.

The choice of the primal unknowns is highly relevant for adequately writing the inverse problem used in the characterization of the viscoelastic material. In this work, novel primal unknowns M and δ, based on the longitudinal wavenumber of the time-harmonic viscoelastic model and the thickness of the material layer, has been used in combination with a data-driven approach where the Young's modulus is assumed an arbitrary frequency-dependent function. With the proposed data-driven approach, the predicted values present a good agreement with the experimental data and avoid spurious oscillatory behaviour. A trust-region reflective algorithm has been used to solve the associated inverse problem. This algorithm requires the computation of the gradient of the cost function to be minimized in the inverse problem.

Finally, some numerical simulations have been performed. The proposed data-driven approach has been validated by using manufactured data. Despite the ill-posedness of the inverse problem in a framework with a very limited amount of data, this test-case scenario has also been used to illustrate the robustness of the method and its accuracy in comparison with well-known parametric models such as the Kelvin-Voigt model. Finally, a real-world viscoelastic material has been characterized, considering a parametric model and the proposed data-driven approach. The numerical results with both methodologies have been compared, showing that the proposed method exhibits smooth frequency response for the Young's modulus, and simultaneous achieves relative errors around 3%, much lower than the classical parametric model.

Declaration of competing interest

The authors declare that they have no known competing financial interests or personal relationships that could have appeared to influence the work reported in this paper.

Data availability

No data was used for the research described in the article.

Acknowledgements

The second author has been supported by MICINN & ERDF project PID2019-108584RB-I00 and ED431C2018/33 - M2NICA (Xunta de Galicia & ERDF). The first author acknowledges funding from the Spanish Ministry of Universities and the European Union-Next GenerationEU under the project RSU.UDC.MS15. The first author is a member of the GNCS group of INdAM.

References

[1] Precision Acoustic. Aptflex SF5048 data sheet. http://acoustics.co.uk/products/acoustic-absorbers-syntactic-foams/anechoic-absorbers/apltile-sf5048 [Online; Last accessed: 19th December 2022].
[2] Allard JF, Atalla N. Propagation of sound in porous media: modelling sound absorbing materials. John Wiley & Sons; 2009.
[3] Amabili M, Balasubramanian P, Breslavsky I. Anisotropic fractional viscoelastic constitutive models for human descending thoracic aortas. J Mech Behav Biomed Mater 2019;99:186–97. https://doi.org/10.1016/j.jmbbm.2019.07.010. ISSN 1751-6161.
[4] Bagley RL, Torvik PJ. On the fractional calculus model of viscoelastic behavior. J Rheol 1986;30(1):133–55. https://doi.org/10.1122/1.549887.
[5] Beamiss GA, Hayman G, Robinson SP. The provision of standards for underwater acoustics at simulated ocean conditions by use of the NPL acoustic pressure vessel. NPL report. National Physics Laboratory; 2001.
[6] Belogol'skii VA, Sekoyan SS, Samorukova LM, Stefanov SR, Levtsov VI. Pressure dependence of the sound velocity in distilled water. Meas Tech 1999;42(4):406–13. https://doi.org/10.1007/BF02504405.
[7] Bergmann L. Der Ultraschall. S. Hirzel, Stuttgart, 6th edition; 1954.
[8] Brekhovskikh LM. Waves in layered media. 2nd edition. Applied mathematics and mechanics, vol. 16. Academic Press; 1980.
[9] Carbajo J, Prieto A, Ramis J, Río-Martín L. A non-parametric fluid-equivalent approach for the acoustic characterization of rigid porous materials. Appl Math Model 2019;76:330–47. https://doi.org/10.1016/j.apm.2019.05.046.
[10] Christensen RM. Theory of viscoelasticity. 2nd edition. Dover civil and mechanical engineering. Dover Publications; 2013.
[11] Coleman TF, Li Y. An interior, trust region approach for nonlinear minimization subject to bounds. SIAM J Optim 1996;6(2):418–45. https://doi.org/10.1137/0806023.
[12] Colleman TF, Li Y. On the convergence of interior-reflective Newton methods for nonlinear minimization subject to bounds. Math Program 1994;67(2):189–224. https://doi.org/10.1007/BF01582221.
[13] Colleman TF, Li Y. A reflective Newton method for minimizing a quadratic function subject to bounds on some of the variables. SIAM J Optim 1996;6(4):1040–58. https://doi.org/10.1137/S1052623494240456.
[14] Conti S, Müller S, Ortiz M. Data-driven problems in elasticity. Arch Ration Mech Anal 2018;229(1):79–123. https://doi.org/10.1007/s00205-017-1214-0.
[15] Cuevas A, Febrero M, Fraiman R. Robust estimation and classification for functional data via projection-based depth notions. Comput Stat 2007;22(3):481–96. https://doi.org/10.1007/s00180-007-0053-0.
[16] Febrero-Bande M, de la Fuente MO. Statistical computing in functional data analysis: the R package fda.usc. J Stat Softw 2012;51(i04). https://doi.org/10.18637/jss.v051.i04.
[17] Ferry JD. Viscoelastic properties of polymers. Wiley; 1980.
[18] Flügge W. Viscoelasticity. A blaisdell book in solid mechanics. Blaisdell Publishing Company; 1967.
[19] Franchini G, Breslavsky ID, Holzapfel GA, Amabili M. Viscoelastic characterization of human descending thoracic aortas under cyclic load. Acta Biomater 2021;130:291–307. https://doi.org/10.1016/j.actbio.2021.05.025. ISSN 1742-7061.
[20] Franchini G, Giovanniello F, Amabili M. Viscoelasticity of human descending thoracic aorta in a mock circulatory loop. J Mech Behav Biomed Mater 2022;130:105205. https://doi.org/10.1016/j.jmbbm.2022.105205. ISSN 1751-6161.
[21] González D, Chinesta F, Cueto E. Consistent data-driven computational mechanics. AIP Conf Proc 2018;1960(1):090005. https://doi.org/10.1063/1.5034931.
[22] Gurtin ME, Sternberg E. On the linear theory of viscoelasticity. Arch Ration Mech Anal 1962;11(1):291–356. https://doi.org/10.1007/BF00253942.
[23] Humphrey VF, Berktay HO. The transmission coefficient of a panel measured with a parametric source. J Sound Vib 1985;101(1):85–106. https://doi.org/10.1016/S0022-460X(85)80040-7.
[24] International Association for the Properties of Water and Steam. IAPWS R6-95. Revised release on the IAPWS formulation 1995 for the thermodynamic properties of ordinary water substance for general and scientific use. In: Proceedings of the 15th international association for the properties of water and steam; 2018.
[25] Jayakumari VG, Shamsudeen RK, Ramesh R, Mukundan T. Modeling and validation of polyurethane based passive underwater acoustic absorber. J Acoust Soc Am 2011;130(2):724–30. https://doi.org/10.1121/1.3605670.
[26] Junglas P. Implementing the IAPWS-95 standard in MATLAB. In: Proceedings of the 15th international conference on the properties of water and steam; 2008.
[27] Kim SY, Lee DH. Identification of fractional-derivative-model parameters of viscoelastic materials from measured FRFs. J Sound Vib 2009;324:570–86. https://doi.org/10.1016/j.jsv.2009.02.040.
[28] Kirchdoerfer T, Ortiz M. Data-driven computational mechanics. Comput Methods Appl Mech Eng 2016;304:81–101. https://doi.org/10.1016/j.cma.2016.02.001.
[29] Krautkrämer J, Krautkrämer H. Ultrasonic testing of materials. Springer; 1990.
[30] Landau LD, Lifshitz EM. Fluid mechanics. Pergamon Press; 1987.
[31] Larbi W. Numerical modeling of sound and vibration reduction using viscoelastic materials and shunted piezoelectric patches. Comput Struct 2017:105822. https://doi.org/10.1016/j.compstruc.2017.07.024.
[32] Le Guisquet S, Amabili M. Identification of the viscoelastic properties of a hydrogel in sol-gel transition by vibration experiments. J Mech Phys Solids 2023;171:105152. https://doi.org/10.1016/j.jmps.2022.105152. ISSN 0022-5096.
[33] Mainardi F. Fractional calculus and waves in linear viscoelasticity. An introduction to mathematical models. Imperial College Press; 2010.
[34] Mesquita AD, Coda HB. A boundary element methodology for viscoelastic analysis: Part I with cells. Appl Math Model 2007;31(6):1149–70. https://doi.org/10.1016/j.apm.2006.04.006.
[35] Meyers MA, Chawla KK. Mechanical behavior of materials. Cambridge University Press; 2008.

[36] Ohayon R, Soize C. Structural acoustics and vibration: mechanical models, variational formulations and discretization. Elsevier Science; 1998.
[37] Rade D, Deü JF, Castello D, Lima AMG, Rouleau L. Passive vibration control using viscoelastic materials. Springer International Publishing; 2019. p. 119–68.
[38] Ramsay J, Ramsay J, Silverman BW. Functional data analysis. Springer series in statistics. Springer; 2005.
[39] Rao MD. Recent applications of viscoelastic damping for noise control in automobiles and commercial airplanes. J Sound Vib 2003;262(3):457–74. https://doi.org/10.1016/S0022-460X(03)00106-8.
[40] Valvano S, Orlando C, Alaimo A. Design of a noise reduction passive control system based on viscoelastic multilayered plate using PDSO. Mech Syst Signal Process 2019;123:153–73. https://doi.org/10.1016/j.ymssp.2019.01.011.